Dragonfly (Sympetrum flaveolum) flight : kinematic measurement and modelling

Chen, Y. H.; Martin, Skote.; Zhao, Y.; Huang, W. M.

2013

Chen, Y. H., Martin, S., Zhao, Y., & Huang, W. M. (2013). Dragonfly (Sympetrum flaveolum) flight: Kinematicmeasurement and modelling. Journal of Fluids and Structures, 40, 115-126.

https://hdl.handle.net/10356/85659

https://doi.org/10.1016/j.jfluidstructs.2013.04.003

Dragonfly (*Sympetrum flaveolum*) Flight: Kinematic Measurement and Modelling

Y.H. Chen[1], M. Skote[1*], Y. Zhao[1,2], and W.M. Huang[1]

[1]School of Mechanical and Aerospace Engineering, Nanyang Technological University, 50 Nanyang Avenue, Singapore 639798

[2]Pressent address: College of Engineering, Alfaisal University,

Al Maathar Road, P.O. Box 50927, Riyadh 11533, Kingdom of Saudi Arabia

[*] Corresponding author, Tel: (+65) 67904271, Fax: (+65) 67904062,

E-mail: mskote@ntu.edu.sg.

Abstract

The kinematics of the flapping hindwing of the dragonfly *Sympetrum flaveolum* is investigated. Several tracking points along the leading edge and trailing edge of the hindwing are recorded and studied using high-speed videography. By applying more tracking points along the leading edge around the nodus, it is shown that the leading edge is not one rigid piece, but two pieces hinged at the nodus with physical constraint of forty degrees. Such arrangement also eases the difficulties in rotating the wing during pronation by bending the leading edge forward and flattening the wing. From the kinematic experiments, two flapping patterns of the dragonfly wing are revealed as a simple figure-eight and a double figure-eight flapping pattern. Kinematic modelling of the two flapping patterns is then established by transforming the flapping motions into angular rotations about the pivoting wing root in a local body-fixed spherical coordinate system.

Keywords: wing kinematics, flapping trajectory, nodus mobility, dragonfly flight

1. Introduction

Amongst various small flying insects, dragonflies possess one of the most manoeuvrable flights. They are capable of developing fast forward flight, hovering and backward flight. Dragonflies operate each of their wings independently (Nagai et al., 2009; Somps and Luttges, 1985; Thomas et al., 2004), and the wing motion is readily controlled by the wing root muscles only (Dickinson et al., 1993; Sunada et al., 1998), making dragonfly an easier target for replicating its wing motions. Bionic Micro-air-vehicles (MAVs) with the flight capabilities like dragonflies have a wide range of applications, such as military reconnaissance, search and rescue et al. In

order to mimic the effective dragonfly flight, the bionic model has to be built with similar functional structures and incorporated with the actual in-flight flapping kinematics. Thus, detailed studies of dragonfly wing kinematics are critical and necessary in understanding the aerodynamics of dragonfly flight, which in turn facilitates the simulation and design of MAVs.

Techniques for determining the wing kinematics of small insect wings and aerofoils alike have been developed in the past decades (Ghommem et al., 2012; Liu, 2009; Wakeling and Ellington, 1997; Walker et al., 2009c; Wang et al., 2003). High speed photography and videography have been widely used in kinematic and flow visualisation of insect flights (Daniel, 1988; Daniel and Combes, 2002; Dudley and Ellington, 1990; Ellington, 1984; Ellington et al., 1996; Walker et al., 2009a, 2009b; Wang, 2003). Often the wings were assumed to be a rigid continuum in structural models (Birch et al., 2004; Dickinson et al., 1999; Kesel, 2000; Okamoto, 1996; Sane and Dickinson, 2001; Smith and Zenieh, 1996) as well as computational models (Sun and Lan, 2004; Wang and Sun, 2005; Xu et al., 2006). However, it is unlikely that the dragonfly wings can be modelled and studied as one rigid piece. Many prior studies consider the flexibility of insect wings (Chen et al., 2013; Combes and Daniel, 2001, 2003a, 2003b, 2003c; Ho et al., 2003; Miao and Ho, 2006; Nakata, 2009; Nakata and Liu, 2009; Young et al., 2009), but none has challenged the implications of a flexible leading edge.

In our research, we carry out detailed kinematic studies on the hindwing of the dragonfly *Sympetrum flaveolum*. The kinematics of the flapping wings are studied through experimentally tracking of the characteristic features including the nodus, the pterostigma and a trailing edge point on the wing instead of the frequently reported wing tip path, using high-speed videography (Please refer to Fig. 1 for a detailed description of the various points on the wing). By taking three points along the wing's leading edge, focused around the nodus, the bending of the leading edge at the nodus is examined. Through our analysis, the leading edge of the dragonfly hindwing is found to be best represented with two relatively rigid pieces hinged at the nodus with a limited degree of rotational freedom.

In general, the fore- and hind-wing pairs in dragonflies are controlled independently and passively at the respective wing root (Nagai et al., 2009; Somps and Luttges, 1985). Computational studies have found that fore- and hind-wing

interaction is detrimental to the vertical force generation (Wang and Sun, 2005); and the tandem configuration does not affect the force and vortex development on the fore-wing, nearly all variations in the aerodynamic performance are attributed to the vortex interaction on the hind-wing (Rival et al., 2011). In addition, since changes in hindwing motion have more effect on changes in the aerodynamic output of the wings than that of the forewing (Nagai et al., 2009; Wakeling and Ellington, 1997), the present study focus on the flapping motion of the hindwing. Moreover, in order to maintain the high shutter speed and resolution of the recording, only the hindwing of the dragonfly are recorded and analysed thoroughly for the flapping patterns. For a complete research, both fore- and hind-wings need to be studied. Maybury and Lehmann (2004) studied the aerodynamic interaction between two robotic wings using the alignment of dragonfly wings. Their experimental results indicated hindwing lift modulation due to fore- and hind-wing interactions. In terms of the kinematics of the robotic wings, the horizontal wing trajectories of the wings were derived from a Fourier series, which is in accordance with our findings and those of others (Wakeling and Ellington, 1997; Wang, 2003). The stroke kinematics they used were adopted from an analytical model based on a single wing simulation (Wang, 2000), and were applied to both fore- and hind-wings. Therefore, a study of the hindwing flapping pattern is both tenable and usable; a generalised kinematic model of a single wing can be applied to both fore- and hind-wings in later mechanical and computational modelling of dragonfly wings.

The focus of the present investigation is on the kinematic measurement and modelling of different flapping patterns in dragonflies, rather than the fore- and hind-wing interactions. Hence, in this investigation, we limit ourselves to the analysis of the hindwing, for the above-stated reasons.

Two different flapping patterns are observed during the in-flight kinematic experiments of the dragonfly: the simple figure-eight (S8) and the double figure-eight (D8) flapping pattern. The S8 flapping pattern has previously been reported in both tethered and free flights of dragonflies (Wakeling and Ellington, 1997; Wang, 2005); whereas the D8 flapping pattern has been observed for other flapping insects (Ellington, 1984) but has so far been only vaguely defined in dragonflies.

In this paper, the two flapping patterns (S8 and D8) are clearly observed and thoroughly analysed, and the three-dimensional (3-D) movements of the flapping

wings are expressed as kinematic models in a local body-fixed coordinate system that we established. Such kinematic modelling facilitates the computational modelling of flapping dragonflies, so that the simulations closely mimic the live dragonfly flight. The kinematic experiments and analysis is presented in the following Section 2; the kinematic modelling is established in Section 3; and we conclude the paper in Section 4.

2. Material and Methods

In this paper, the insect used for all the following studies is the dragonfly, yellow-winged darter *Sympetrum flaveolum*. The dragonflies were caught alive near Nanyang Lake in Nanyang Technological University, Singapore.

2.1. Critical points for the flapping trajectories

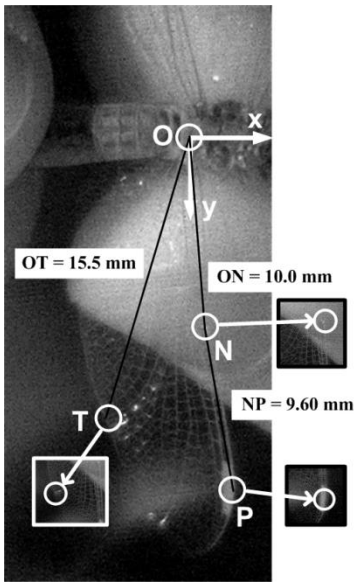

Fig. 1. The image of the dragonfly hindwing with critical tracking points *O*, *N*, *P* and *T*, where *O* is at the wing root, *N* is at the nodus, *P* is at the middle of the pterostigma and *T* is at the intersection of the anterior median vein (*MA*) and the trailing edge of the hindwing.

Before filming, four critical points (*O*, *N*, *P* and *T*) were identified on the hindwing as demonstrated in Fig. 1. These four points were chosen as the tracking points for the flapping trajectories because of their excellent visibility on the transparent wing. They were easily identified in the black and white film without the need to use any artificial paints to mark them out on the wing.

2.2. Filming

Photron high-speed video camera Fastcam X-1024 PCI was used in the experiment to capture and record the flapping motion of a tethered dragonfly. The

dragonfly was held on the legs and tail by fingers, which is the easiest way to hold the dragonfly and to further adjust its positioning. Care was taken when holding the insect to make sure its body did not wobble and the fingers did not interfere with the wings during flapping. In general, due to the restriction on the dragonfly wing root muscles, dragonfly wings are unable to touch each other at the dorsal or ventral most position, and the wing motion are more restricted relative to the insect body (Wakeling and Ellington, 1997; Wootton, 1992). Hence, the fingers holding to the legs are less likely to invade the flapping wings. In addition, since the size of the fingers holding the insect is smaller than one-third of the wing length (refer to Fig.1), the proximity of the fingers should not alter the wing tip vortices; in other words, the aerodynamic ground effects are less likely to affect our in-flight kinematic measurements.

An insect in free flight has six degrees of freedom including rolling, pitching and yawing for the body movements, as well as, elevating, feathering and positioning for the wing movements. A flapping flight with so many degrees of freedom is difficult to comprehend and quantify. Therefore, the next best method seems to be to deprive the insect of a certain degree of freedom and thus create conditions for measuring. In this case we fixed the body of the dragonfly, hence depriving it of the freedom of motion on the body level, and were thus able to focus on the wing movements about the wing root. Moreover, tethered flights are not necessarily unrealistic. Recent free flight recordings of dragonflies (Thomas et al., 2004; Wakeling and Ellington, 1997) provide us baseline data for comparison (detailed comparison in Section 2.4.1). Using the free flights as guidelines, we are able to restrict our analysis of tethered flights to those matching free flights. Hence, we are reducing the difficulties in quantifying a high degree of freedom movement, as well as keeping the motion as realistic as possible.

Furthermore, caution was exercised when calibrating the high-speed camera to ensure the focus plane (at the lens) was parallel with the insect body plane (Clarke et al., 1998). The high-speed video camera was calibrated every time before use, and set to 6000 frames per second (fps) with a resolution of 256×512 pixels. Such shutter speed and resolution are higher than that of previous studies.

2.3. Kinematic analysis

The flapping motion is studied using the corresponding software, Photron Motion Tools, with a sequential frame analysis. The accuracy of such analysis mainly

depends on the shutter speed and resolution of the film. By taking 6000 fps, we are able capture one complete flapping cycle with around 150 frames. With these numbers of frames, the uncertainty of our method of frequency measurement is limited to an error of 0.7% per flapping cycle, which doubles the accuracy of Wakeling and Ellington (1997). Even the rapid rotational phases (pronation and supination) can be measured with less than ± 2° error. Moreover, due to the high frame rate, the changes in the wing position from one frame to another are minimal, so that the error of reconstructing the wing positions is limited to within ± 1°.

2.3.1. Coordinate systems fixed on the body

The tracking points were viewed in a global 2-D coordinate system first, then converted into a local body-fixed 3-D Cartesian coordinate system as shown in Fig. 2(a), and further converted into a local body-fixed 3-D spherical coordinate system as shown in Fig. 2(b). The films of the flapping wing were 2-D images taken from a single viewing direction by placing the camera lens parallel to the dragonfly body plane. These images were digitised in a global *x*-*y* coordinate system with both the *x* and *y* axes parallel to the filming plane. The *x* axis is horizontal and the *y* axis is vertical as shown in Fig. 1.

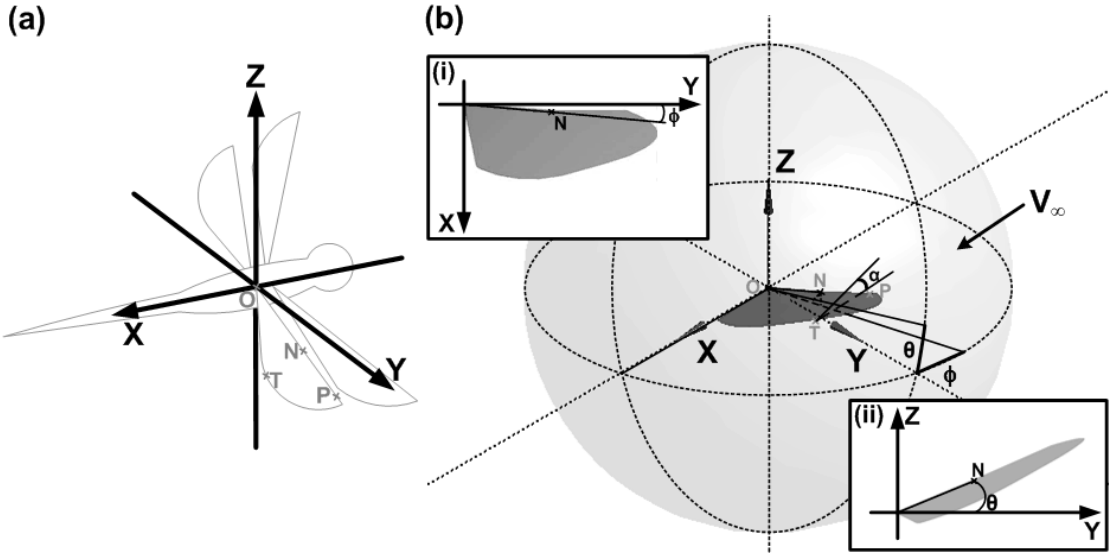

Fig. 2. The local body-fixed Cartesian and spherical coordinate systems. (a) The local body-fixed Cartesian coordinate system shown on the dragonfly hindwing. The origin is at the wing root. *X* axis passes through the wing root and is parallel to the longitudinal axis of the dragonfly body. Both *Y* and *Z* axes are perpendicular to *X* axis, with *X* and *Y* forming the filming plane which is parallel to the camera lens, and *Z* normal to the filming plane and pointing into the lens. *O*, *N*, *T* and *P* on the hindwing indicate the corresponding position of the wing root, the nodus, the trailing edge point and the pterostigma at any instant of the flapping cycle respectively. (b) The local body-fixed spherical coordinate system (ϕ, θ). α is the geometric angle of attack at *T* with respect to the free-stream velocity in the *X*-direction. (i) The position angle ϕ is the acute angle between the positive *Y*-axis and the

projection of the leading edge on the *X*-*Y* plane. ϕ is positive along the negative *X*-axis, and negative along the positive *X*-axis. (ii) The elevation angle θ is the acute angle between the positive *Y*-axis and the projection of the leading edge on the *Y*-*Z* plane. θ is positive above *X*-*Y* plane, and negative below it.

As illustrated in Fig. 2(a), the origin of the local body-fixed 3-D Cartesian coordinate system is set at the wing root of one of the dragonfly hindwings. *X* axis is passing through the wing root and parallel to the longitudinal axis of the dragonfly body. Both *Y* and *Z* axes are perpendicular to *X* axis, with *X* and *Y* forming the filming plane parallel to the camera lens, and *Z* axis normal to the filming plane but pointing into the lens. *O*, *N*, *T* and *P* on the hindwing indicate the corresponding position of the critical points demonstrated in Fig. 1 at any instant of the flapping cycle. Since the insect body is held still, the wing root position remains the same during flapping.

When the wing flaps, its orientation keeps changing with respect to the filming plane, so that the projected lengths of *ON*, *NP* and *OT* change accordingly. During one wing-beat cycle, the wing passes through a position where it is parallel to the filming plane and gives the maximum projected wing length (Wakeling and Ellington, 1997). The maximum projected wing length captured in a film image represents scale multiples of the actual wing length, and that position should be considered as the reference plane (Ellington, 1984). By comparing the actual wing length and the maximum projected length measured at the reference plane, this scale multiple is obtained. As the origin of the local body-fixed 3-D Cartesian coordinate system is at the wing root, the digitised global *x*-*y* coordinates are adjusted into the new local body-fixed *X*-*Y* coordinates by zeroing at the wing root point *O*. Therefore, only *Z* coordinates are unknown for the new coordinate system.

Considering the relative rigidity of the leading edge and the anterior median vein, it is reasonable to assume that the lengths of *ON*, *NP* and *OT* do not change noticeably during flapping. As seen in Fig. 1, the movement of the leading edge spar is tracked with two variables *N* and *P*. Therefore, the leading edge is divided into two sections; *ON* and *NP*. The rigidity of the leading edge spar is then challenged by analysing the angle formed at the nodus (*N*) with *ON* and *NP*. If the angle is kept around zero degrees, then there is no bending of the leading edge, in other words, the leading edge is one rigid spar. However, if the angle *ONP* changes with time, then the leading edge spar is not rigid. In addition, due to the high shutter speed of 6000 fps, the changes in

the wing position from one frame to another are minimal, making the assumption of rigid vein sections possible.

The corresponding orientation of the hindwing at points *N*, *P* and *T* can be calculated from the known maximum projected length and the digitised *X* and *Y* coordinates as:

$$Length = \sqrt{\left(X_2 - X_1\right)^2 + \left(Y_2 - Y_1\right)^2 + \left(Z_2 - Z_1\right)^2}\,, \tag{1}$$

so that

$$Z_2 = \sqrt{Length^2 - \left(X_2 - X_1\right)^2 - \left(Y_2 - Y_1\right)^2} + Z_1\,, \tag{2}$$

where the subscripts 1 and 2 represent *O* and *N* respectively when calculating the length *ON*; *N* and *P* when dealing with *NP*; and, *O* and *T* when calculating *OT*. Thus the value of the *Z* coordinates can be evaluated, whereas the direction of *Z* is determined by careful observation from the film.

Figure 2(b) demonstrates the local body-fixed spherical coordinate system (ϕ, θ) established for kinematic modelling. As shown by the inserts (i) and (ii) in Fig. 2(b), the position angle ϕ is the acute angle between the positive *Y*-axis and the projected line of the leading edge on the *X*-*Y* plane, and the elevation angle θ is the acute angle between the positive *Y*-axis and the projected leading edge on the *Y*-*Z* plane. α is the geometric angle of attack, determined at 60% wing length (point *T*) with respect to the free-stream velocity in *X*-direction. It is positive when the leading edge is above the trailing edge and negative when the trailing edge is above the leading edge.

In the present studies of dragonflies, the flapping motion is essentially wing rotations initiated from the wing root. Thus, the wing motion is best described by locating the wing position via the position angle ϕ and the elevation angle θ of the leading edge, and then adjusting the wing attitude via the geometric angle of attack α. In such way, a flapping flight can be effectively captured at every time instant. Therefore, converting the local body-fixed Cartesian coordinate system into the local body-fixed spherical coordinate system is vital for establishing a working kinematic modelling.

2.3.2. Comparison of trajectories with Wakeling and Ellington's

For a more clear illustration, the trajectories shown in Figs 3 and 4 represent the projected positions of the tracking points onto the *X*-*Z* plane as if viewed from the

side of the dragonfly wing. One of most resourceful and fundamental kinematic studies in the literature of dragonfly flight is from Wakeling and Ellington (1997). They studied the wing-tip trajectories of free flying dragonflies. By aligning the present local body-fixed coordinate system with that of Wakeling and Ellington (1997) at the wing root, the present flapping trajectory near wing tip (at the pterostigma) with S8 trajectory can be superimposed on their wing-tip trajectory.

As seen in Fig. 3, it is clear that the two trajectories share many similar trends. Firstly, they have about the same stroke amplitude. Secondly, the trajectories coincide very well at downstroke, and only differ slightly at upstroke. Thirdly, both the crossings of the trajectories occur near pronation. Moreover, the density of the data points (with the same time interval) is more intense around pronation and supination for both cases, which indicates that speed in rotational motion is faster than that of translational motion in a flapping wing. In addition, the stroke plane of both trajectories is about the same, with our tethered flight less than 2^{o} forward to the horizontal as compared to the free flight.

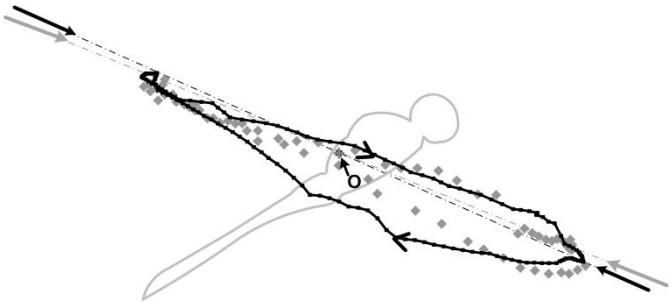

Fig. 3. Comparison of the present flapping trajectory at the pterostigma with the wing-tip path from Wakeling and Ellington (1997). *O* indicates the wing root. The stroke plane is indicated by a line connecting the two opposing arrows through the wing root. The distance from the cross to the tip of either arrowhead indicates the wing length. The arrows on the trajectory indicate the forward direction of the wing motion. The grey diamonds marked the hindwing wing tip position from Wakeling and Ellington (1997), while the black connected line shows near wing tip trajectory of the current study.

The tethered flight conditions are not identical to free flights. However, the similarities demonstrated in the above comparison encourage us in using the limited tethered flight setup to reduce the difficulties in quantifying a high degree of freedom movement, as well as keeping the motion as realistic as possible by consulting the free flights as guidelines. In our experiments, the flapping trajectory is tracked at the nodus besides the near wing tip pterostigma. One complete flapping cycle starts with the wing positioning horizontally and levelling with the insect body and ends when

the wing moves back to that horizontal position again. Typical flapping patterns are depicted in the next section, and later characterised in the kinematic modelling.

2.3.3. Flapping trajectories at the nodus and the pterostigma

Five flapping cycles are analysed in detail. For the flapping trajectories at nodus and pterostigma, three out of five cycles demonstrate simple figure-eight trajectories. However, the remaining two cycles depict a double figure-eight flapping trajectory. Figure 4 illustrates how the two distinct flapping patterns occur in sequence. The experiment was carried out on living organisms; the flapping motions were unlikely to repeat with exact trajectories. The key is to identify the characteristic feature, which leads to the naming of the distinct flapping patterns. The characteristic feature differentiating the two different trajectories is the cross-over of the flapping path at stroke reversals. There is only one cross-over for the simple figure-eight trajectory, and the flapping path resembles a (distorted) figure-eight, thus the naming. On the other hand, there are two cross-overs for the so-named double figure-eight trajectory.

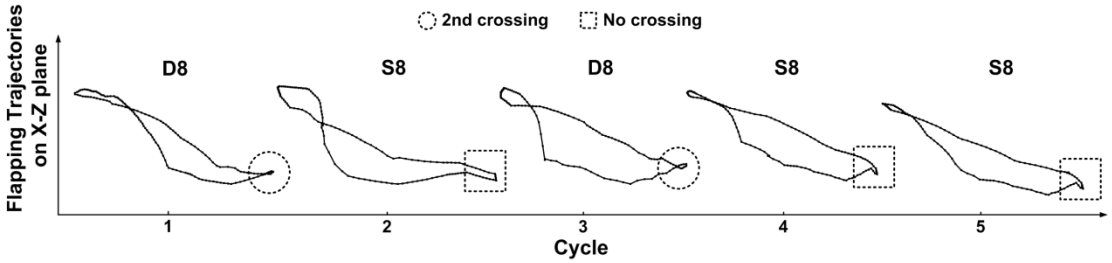

Fig. 4. Flapping trajectories of the nodus in five consecutive flapping cycles. Dotted circle indicates the second crossing, and dotted square, no crossing. D8 denotes double figure-eight trajectory, and S8, simple figure-eight trajectory.

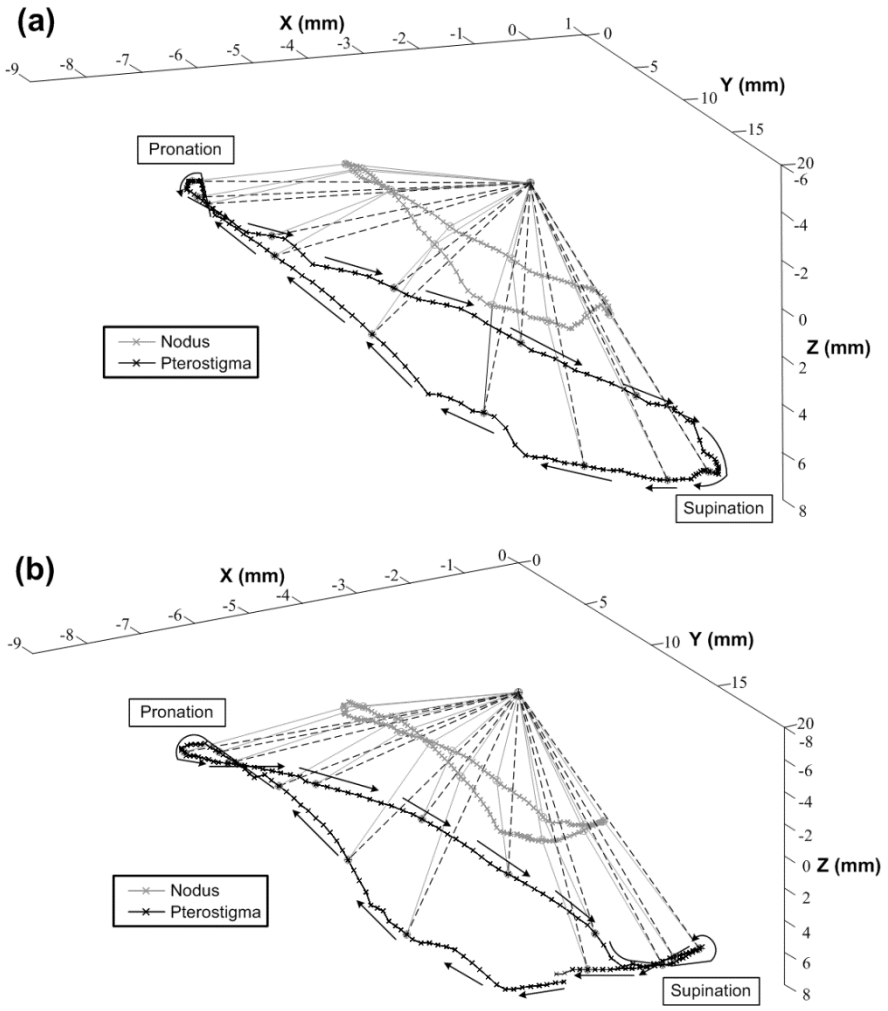

Fig. 5. Typical flapping trajectories at the nodus and the pterostigma. The black broken lines connect the wing root to the pterostigma, while the grey solid lines connect the wing root to the nodus and the pterostigma at the same time instant. (a) Simple figure-eight (S8) flapping trajectories. (b) Double figure-eight (D8) flapping trajectories.

Two typical cases are presented in Fig. 5 for the simple figure-eight and double figure-eight flapping trajectory, respectively. The trajectories of both the nodus and the pterostigma are similar in the two different flapping patterns. Comparing Fig. 5(a) and (b), similar trends are observed for the translational phases of the simple figure-eight and double figure-eight patterns, while differences mainly occur during rotational phases, especially during supination. The flapping trajectories always cross over during pronation, but not always cross over during supination. It is precisely this difference that determines whether the pattern is named simple figure-eight or double figure-eight.

There seems to be no fixed rules for the switching between different flapping patterns. Studies have shown that free-flying insects often use different aerodynamic

mechanisms in successive flapping cycles; they are free to choose from different mechanisms for the same flapping process (Srygley and Thomas, 2002). One possible interpretation is that the dragonfly uses different flapping patterns to achieve different aerodynamic effects.

3. Results and Discussion

3.1. Kinematic measurement

The downstroke-to-upstroke ratio *d*/*u* has an average value of 2.24 for the hindwing, with 68 % of downstroke and 32 % upstroke. Pronation and supination are approximately equal in duration. The wing rotates through a relatively moderate angle during pronations and supinations as compared to the large angle of 110° observed by Ellington (1984) in various hovering insects. Typically the change in geometric angle of attack is more pronounced in pronations, which gives rise to an average angular change of 38^o whereas it is 36^o for supinations.

3.1.1. Flapping frequency

For our tethered dragonfly flight, the flapping frequency *n* remains reasonably consistent for all the wing-beat cycles with a mean value of 39 Hz, which is within the range from 36 Hz (Tsuyuki, 2006) to 44 Hz (Wakeling and Ellington, 1997) found for free flight.

3.1.2. Bending of the leading edge spar

By taking two tracking points at the leading edge, deformation on the leading edge can be investigated. As shown in Fig. 1, the angle *ONP* is the angle formed by the leading edge section *ON* and *NP* at the nodus. With the 3-D Cartesian coordinates established in Section 2.3.1, the 3-D angle *ONP* is obtained. The angle *ONP* is slightly bending forward even at its resting position, so that the smallest value of the angle corresponds to the leading edge position when it bends the most forward. Figure 6 demonstrates how angle *ONP* changes with time as well as that of the distance from the wing root to the pterostigma *OP*. Both the angle *ONP* and distance *OP* change with time, which strongly suggests that the leading edge spar is not a rigid one piece. Three flapping cycles are shown in Fig. 6. Both smallest values of the angle *ONP* and distance *OP* correspond to the onset of pronation, while the largest and almost constant values correspond to the supination period.

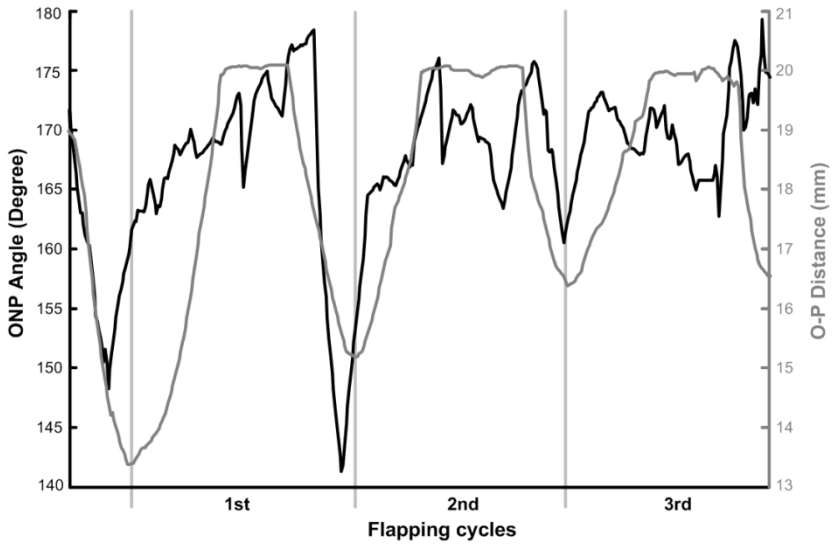

Fig. 6. Changes of angle *ONP* (black line) and distance *OP* (grey line) with respect to three flapping cycles.

The angle *ONP* is largest and almost kept constant during supination so that the ventral camber is maintained to facilitate the rotation. Since it is well known that the muscle control of small insects such as dragonflies is restricted to the wing root, the bending of the leading edge cannot be actively controlled. There must be some other ways to control the bending angles of the leading edge. The nodus was suspected to work as a hinge by Sudo without in-flight experimental results to support it (Sudo et al., 1999). From Fig. 6, it is noted that the angle *ONP* changes over a range of 40^{o}, which will probably cause buckling failure of the leading edge if it is a rigid one piece. On the other hand, if the nodus is a hinge with an L-shaped stopper to restrain its freedom of rotation to approximately 40^{o}, together with any aerodynamic forces acting on the wing, it will control the bending and rotation of the wing during pronation and supination. Hence, we suggest that the leading edge spar is not a rigid one-piece but two pieces hinged at the nodus with approximately 40^{o} freedom of rotation.

Furthermore, it is usually presumed that the rotation of the wing during pronation is much more difficult than that of the supination since the wing is ventrally cambered (Ennos, 1988, 1995). Wootton and co-workers have observed that the inverted V-shaped groove on the distal section away from the nodus, typically allowing supinatory twisting while restricting pronatory twisting (Wootton et al., 1998). However, our kinematic analysis shows that the typical change in the geometric angle of attack is more pronounced in pronations, which gives rise to an average angular

change of 38^o whereas it is 36^o for supinations. Referring to Fig. 6, the leading edge of the hindwing bends most forward and starts rotating at the onset of pronation. Hence, the pleated wing surface is stretched and flattened most at this point of time. By bending the leading edge forward and flattening the wing, the wing rotation during pronations is made easier. Thus, it is a common misunderstanding that the wing rotation during pronation is much more difficult than that during supination.

3.2. Kinematic modelling

Since the muscles controlling wing motions in dragonflies are restricted at the wing root, it is reasonable to dissect the wing motions into rotational movements about the pivoting wing root. Thus, the wing motion is best described by locating the wing position via the position angle ϕ and the elevation angle θ of the leading edge, and then adjusting the wing attitude via the geometric angle of attack α. The flapping wing motion at any time instant can be duplicated as long as the required kinematic data is available at that instant.

In the present kinematic modelling, Fourier series are fitted to describe the geometric angle of attack α, the position angle ϕ and the elevation angle θ with time. The first six Fourier terms are used to assess the importance of higher harmonics within the flapping cycle. The acquired flapping cycles for the kinematic modelling correspond to the same S8 and D8 cycles illustrated in Fig. 4 respectively. However, the time t is non-dimensionalised with the period of the flapping cycle T so that the dimensionless time $\hat{t} = t/T$; and a flapping cycle starts at $\hat{t} = 0$ with the wing positioning horizontally and levelling with the insect body (at $\phi = 0$, $\theta = 0$ and $\alpha = 0$), and ends at $\hat{t} = 1$ when the wing moves back to that horizontal position.

3.2.1. Typical time series of the geometric angle of attack

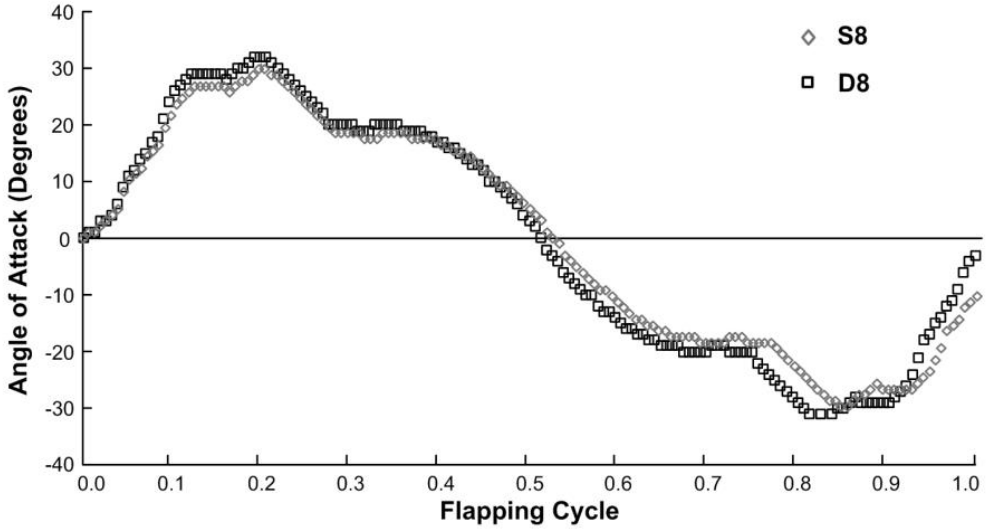

Fig. 7. Time series of the typical geometric angle of attack α of the hindwing during one complete flapping cycle. Grey diamond S8 denotes simple figure-eight flapping pattern; and black square D8 denotes double figure-eight flapping pattern.

In the present analysis, the geometric angle of attack α is determined at 60% wing length where the point *T* is taken at the intersection of *MA* and the trailing edge. As shown in Fig. 3(b), α is the geometric angle of attack at *T* with respect to the free-stream velocity. However, unlike fixed-wing flight, the wing chord is not always aligned with the free-stream velocity in the *X*-direction when the wing flaps. Therefore, the geometric angle of attack α is the angle that the projected wing chord on the *X*-*Z* plane at *T* makes with the free-stream velocity in the *X*-direction. It is positive when the leading edge is on top of the trailing edge and negative when the trailing edge is on top.

The geometric angle of attack is thus calculated from the relative Cartesian coordinates of the leading edge point *N* and the trailing edge point *T* on the *X*-*Z* plane at *T*. A typical cycle of the geometric angle of attack for each flapping pattern is plotted in Fig. 7 with time. As seen from Fig. 7, the different flapping trajectories have not much effect on the variation of the geometric angle of attack. Generally, the geometric angle of attack changes gradually during the two translational phases and remains constant during the middle portion of each half-stroke. During the two rotational phases, the geometric angle of attack changes rapidly with relatively larger amplitude, representing by a steeper gradient as compared to the mild and horizontal gradient during translational phases, as demonstrated in Fig. 7.

Note that there exists a gap in the geometric angle of attack at the end of the time series (about -3^o for D8 and -10^o for S8, respectively) and hence a complete cycle is not achieved. However, the flapping cycle is considered complete once the leading edge has moved back to its original position. During natural flight, this does not always occur at the same time the trailing edge moves back to its horizontal position. Thus, there will always be a small gap in the measurements of a cycle of the geometric angle of attack**.**

3.2.2. Typical time series of the position and elevation angle

The position angle ϕ is positive when the wing is moving towards the head of the insect, and negative when moving towards the tail. The elevation angle θ is positive when the wing is dorsal, i.e., above *X*-*Y* plane; and negative when ventral, below *X*-*Y* plane. With the presumption that the leading edge is rigid with two pieces hinged at nodus, the leading edge is divided into two sections with a basal section from wing root to nodus described by (ϕ_N, θ_N) and a distal section from nodus to wing tip by (ϕ_P, θ_P). Figure 8 illustrates the typical time series of the positional angle ϕ and the elevation angle θ of the two flapping patterns, a simple figure-eight (S8) and a double figure-eight (D8) flapping trajectory. The cross and circle indicate the position angle ϕ and the elevation angle θ of the front wing section from the wing root to the nodus, respectively; the diamond and triangle indicate the position angle ϕ and the elevation angle θ of the back wing section from the nodus to the wing tip, respectively. The difference between the two flapping patterns mainly occurs in the elevation angle during the second half of the flapping cycle.

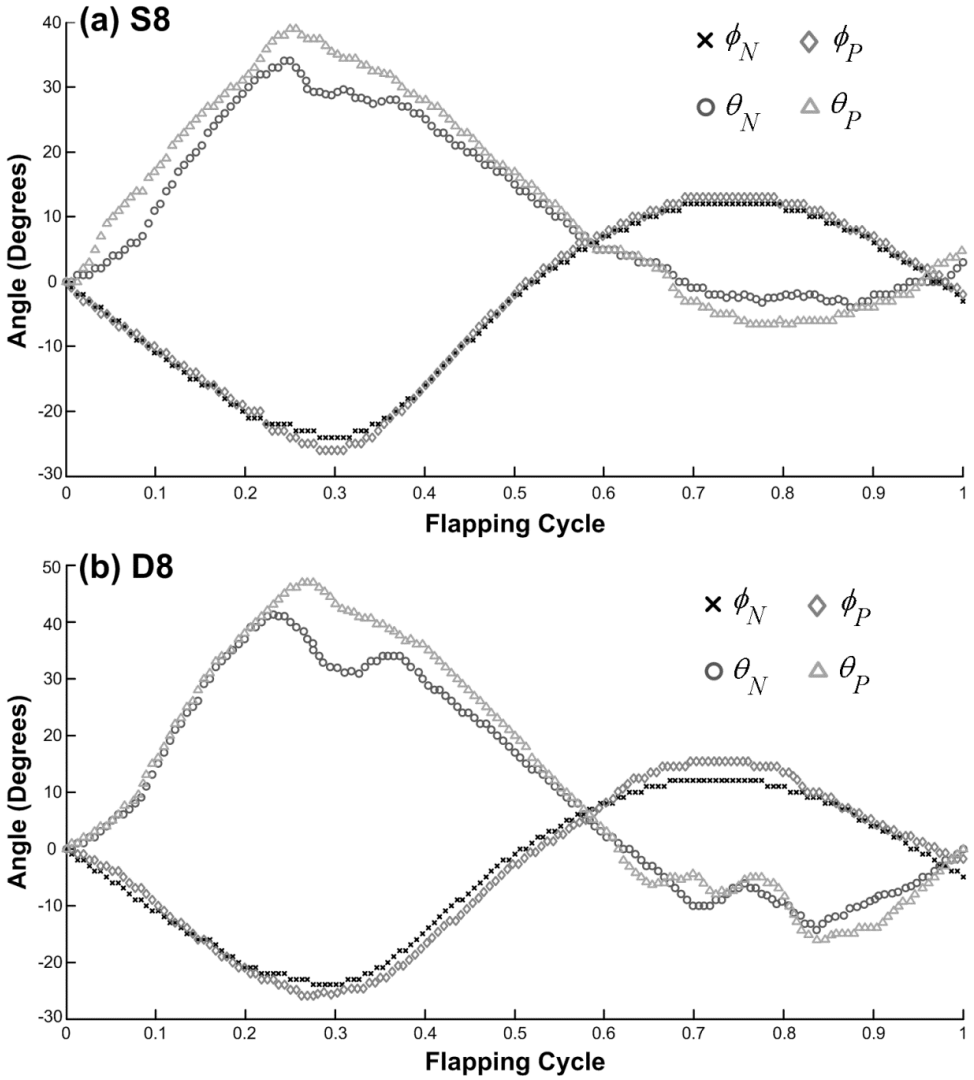

Fig. 8. Time series of the position angle ϕ and the elevation angle θ of the hindwing during one complete flapping cycle for (a) simple figure-eight (S8) trajectory and (b) double figure-eight (D8) trajectory. Cross and circle indicate the position angle ϕ and the elevation angle θ of the wing section from the wing root to the nodus. Diamond and triangle indicate the position angle ϕ and the elevation angle θ of the wing section from the nodus to the wing tip.

3.2.3. Kinematic modelling via Fourier series analysis

In the local body-fixed spherical coordinate system, a kinematic model is established via Fourier series analysis for each flapping pattern. The series were truncated after the sixth harmonic term, which resulted in a smooth fit to the raw data. Approximations using harmonics higher than six produced unrealistic kinks around the data peaks and troughs, which led to excessive angular accelerations. Similar

observations were made in other fitting procedures (Wakeling and Ellington, 1997; Willmott and Ellington, 1997).

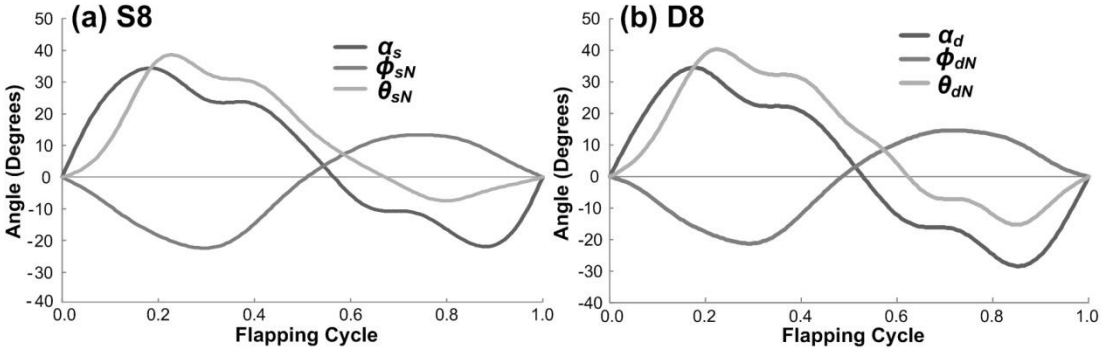

Fig. 9. Time series of the position angle, the elevation angle and the geometric angle of attack of the hindwing during one complete flapping cycle. The curves are the fitted results from the Fourier series analysis of in-flight kinematic data, where the subscript *s* denotes simple figure-eight flapping trajectory, *d*, double figure-eight flapping trajectory, and *N*, nodus. (a) Simple figure-eight (S8) flapping trajectory presented in ϕ_{sN}, θ_{sN} and α_s. (b) Double figure-eight (D8) flapping trajectory presented in ϕ_{dN}, θ_{dN} and α_d.

Fourier series are fitted to the in-flight measurements of the position angle ϕ, the elevation angle θ and the geometric angle of attack α, to describe the changes of these angles with respect to the normalised time. For a clear illustration of the result from the fitting procedure, Figs 9(a) and (b) depict the time series of the geometric angle of attack α and the position of the leading edge at nodus (ϕ_N, θ_N) in a typical simple figure-eight (S8) and double figure-eight (D8) flapping cycle, respectively. Note that Fig. 9 depicts the fitted Fourier series curves from the in-flight kinematic data presented previously in Figs 7 and 8. The full formulation of the kinematic modelling expressed in Fourier series can be found in the appendix.

The difference between the fitted model and the in-flight measurement is expressed in terms of the sum of squares due to error (SSE):

$$\mathrm{SSE} = \sum_{i=1}^{n} \left(y_i - \hat{y}_i \right)^2 , \tag{3}$$

where y_i is the i^{th} value of the data measured in the experiment, $\hat{y}_i$ is the predicted value of y_i, and n is the number of data points within one complete flapping cycle. SSE hence evaluates the total deviation of the fitted values from the observed values.

In the present kinematic modelling, the coefficients of the Fourier series are deemed significant at a 95 % confidence level. The fitted curves of ϕ, θ and α are deemed good as the maximum SSE does not exceed 0.1.

4. Conclusions

Kinematic studies of the dragonfly flight in this paper show that the flapping pattern of a dragonfly hindwing at the nodus and the pterostigma is either a simple figure-eight (S8) or a double figure-eight (D8). The double figure-eight flapping trajectory has never been observed in in-flight experiments of dragonflies, while the simple figure-eight trajectory is similar to that in Wakeling and Ellington (1997). A comparison of the S8 flapping trajectories between Wakeling and Ellington's free flight and our tethered flight shows the effect and reliability of tethered flight.

The bending analysis of the leading edge spar indicates that the leading edge spar is not a rigid one-piece but two pieces hinged at the nodus. At the nodus, the leading edges from the basal and distal wing sections are only able to move (relatively to each other) up to an angle of approximately 40^{o}. Therefore the dragonfly wings are unable to fold as much as that of cockroaches (Haas, 1996). On the other hand, the leading edge of the hindwing bends most forward to flatten the wing, and starts rotating at the onset of pronation, hereby eases the wing rotation during pronations. Thus, it seems to be a common misunderstanding that the wing rotation during pronation is much more difficult than that during supination.

Furthermore, the kinematic modelling of the dragonfly flight is established by expressing the angular rotations (ϕ, θ and α) of the wing about the *Z*-*X*-*Y* axes in the spherical coordinate system via Fourier series. The kinematic model for each flapping pattern (S8 and D8) can be used in computational studies of dragonfly flight by incorporating the in-flight kinematics into the dynamic simulations. As such, we can investigate the changes in the aerodynamic effects caused by the differences of the kinematic flapping patterns alone.

Appendix

In the local body-fixed spherical coordinate system, a kinematic model is established for each flapping pattern. In a typical simple figure-eight (S8) flapping

cycle, the geometric angle of attack α_s and the positions of the leading edge sections (ϕ_{sN} , θ_{sN}) and (ϕ_{sP}, θ_{sP}) are expressed in Fourier series as follows:

$$\alpha_s(\hat{t}) = \sum_{n=0}^{6}\left[\alpha_{san}\cos\left(n\hat{t}\right) + \alpha_{sbn}\sin\left(n\hat{t}\right)\right], \tag{4}$$

$$\phi_{sN}(\hat{t}) = \sum_{n=0}^{6}\left[\phi_{sNan}\cos(n\hat{t}) + \phi_{sNbn}\sin(n\hat{t})\right], \tag{5}$$

$$\theta_{sN}(\hat{t}) = \sum_{n=0}^{6}\left[\theta_{sNan}\cos(n\hat{t}) + \theta_{sNbn}\sin(n\hat{t})\right], \tag{6}$$

$$\phi_{sP}(\hat{t}) = \sum_{n=0}^{6}\left[\phi_{sPan}\cos(n\hat{t}) + \phi_{sPbn}\sin(n\hat{t})\right], \tag{7}$$

$$\theta_{sP}(\hat{t}) = \sum_{n=0}^{6}\left[\theta_{sPan}\cos(n\hat{t}) + \theta_{sPbn}\sin(n\hat{t})\right], \tag{8}$$

where n is an integer changing from 0 to 6; $\hat{t}$ is the dimensionless time; and the coefficients $\alpha_{san,\ sbn}$, $\phi_{sNan,\ sNbn,\ sPan,\ sPbn}$, $\theta_{sNan,\ sNbn,\ sPan,\ sPbn}$ are determined from the measured in-flight kinematic data in Figs 7 and 8(a).

On the other hand, in a typical double figure-eight (D8) flapping cycle, the geometric angle of attack α_d and the positions of the leading edge sections (ϕ_{dN}, θ_{dN}) and (ϕ_{dP}, θ_{dP}) are expressed similarly using Fourier series:

$$\alpha_d(\hat{t}) = \sum_{n=0}^{6}\left[\alpha_{dan}\cos\left(n\hat{t}\right) + \alpha_{dbn}\sin\left(n\hat{t}\right)\right], \tag{9}$$

$$\phi_{dN}(\hat{t}) = \sum_{n=0}^{6}\left[\phi_{dNan}\cos(n\hat{t}) + \phi_{dNbn}\sin(n\hat{t})\right], \tag{10}$$

$$\theta_{dN}(\hat{t}) = \sum_{n=0}^{6}\left[\theta_{dNan}\cos(n\hat{t}) + \theta_{dNbn}\sin(n\hat{t})\right], \tag{11}$$

$$\phi_{dP}(\hat{t}) = \sum_{n=0}^{6}\left[\phi_{dPan}\cos(n\hat{t}) + \phi_{dPbn}\sin(n\hat{t})\right], \tag{12}$$

$$\theta_{dP}(\hat{t}) = \sum_{n=0}^{6}\left[\theta_{dPan}\cos(n\hat{t}) + \theta_{dPbn}\sin(n\hat{t})\right], \tag{13}$$

where n is an integer changing from 0 to 6; $\hat{t}$ is the dimensionless time; and the coefficients $\alpha_{dan,\ dbn}$, $\phi_{dNan,\ dNbn,\ dPan,\ dPbn}$, $\theta_{dNan,\ dNbn,\ dPan,\ dPbn}$ are also determined from the measured in-flight kinematic data in Figs 7 and 8(b).

References

Birch, J. M., Dickson, W. B. and Dickinson, M. H. (2004). Force production and flow structure of the leading edge vortex on flapping wings at high and low Reynolds numbers. Journal of Experimental Biology 207, 1063-1072.

Chen, Y. H., Skote, M., Zhao, Y. and Huang, W. M. (2013). Stiffness evaluation of the leading edge of the dragonfly wing via laser vibrometer. Materials Letters 97, 166-168.

Clarke, T. A., Fryer, J. G. and Wang, X. (1998). The Principal Point and CCD Cameras. Photogrammetric Record 16, 293-312.

Combes, S. A. and Daniel, T. L. (2001). Shape, flapping and flexion: wing and fin design for forward flight. Journal of Experimental Biology 204, 2073-2085.

Combes, S. A. and Daniel, T. L. (2003a). Flexural stiffness in insect wings I. Scaling and the influence of wing venation. Journal of Experimental Biology 206, 2979-2987.

Combes, S. A. and Daniel, T. L. (2003b). Flexural stiffness in insect wings II. Spatial distribution and dynamic wing bending. Journal of Experimental Biology 206, 2989-2997.

Combes, S. A. and Daniel, T. L. (2003c). Into thin air: contributions of aerodynamic and inertial-elastic forces to wing bending in the hawkmoth *Manduca sexta*. Journal of Experimental Biology 206, 2999-3006.

Daniel, T. L. (1988). Forward flapping flight from flexible fins. Canadian Journal of Zoology 66, 630 -638.

Daniel, T. L. and Combes, S. A. (2002). Flexible Wings and Fins: Bending by Inertial or Fluid-Dynamic Forces? Integrative and Comparative Biology 42, 1044-1049.

Dickinson, M. H., Lehmann, F.-O. and Sane, S. P. (1999). Wing Rotation and the Aerodynamic Basis of Insect Flight. Science 284, 1954-1960.

Dickinson, M. H., Lehmann, F. O. and Gotz, K. G. (1993). The active control of wing rotation by *Drosophila*. Journal of Experimental Biology 182, 173-189.

Dudley, R. and Ellington, C. P. (1990). Mechanics of Forward Flight in Bumblebees: I. Kinematics and Morphology. Journal of Experimental Biology 148, 19-52.

Ellington, C. P. (1984). The Aerodynamics of Hovering Insect Flight. III. Kinematics. Philosophical Transactions of the Royal Society of London Series B: Biological Sciences 305, 41-78.

Ellington, C. P., Van den Berg, C., Willmott, A. P. and Thomas, A. L. R. (1996). Leading-edge Vortices in Insect Flight. Nature 384, 626-630.

Ennos, A. R. (1988). The Importance of Torsion in the Design of Insect Wings. Journal of Experimental Biology 140, 137-160.

Ennos, A. R. (1995). Mechanical Behaviour in Torsion of Insect Wings, Blades of Grass and other Cambered Structures. Proceedings of the Royal Society of London Series B: Biological Sciences 259, 15-18.

Ghommem, M., Hajj, M. R., Mook, D. T., Stanford, B. K., Beran, P. S., Snyder, R. D. and Watson, L. T. (2012). Global optimization of actively morphing flapping wings. Journal of Fluids and Structures 33, 210-228.

Haas, F., and Wootton, R. J. (1996). Two Basic Mechanisms in Insect Wing Folding. Proceedings of the Royal Society of London Series B: Biological Sciences 263, 1651-1658.

Ho, S., Nassef, H., Pornsinsirirak, N., Tai, Y.-C. and Ho, C.-M. (2003). Unsteady aerodynamics and flow control for flapping wing flyers. Progress in Aerospace Sciences 39, 635-681.

Kesel, A. B. (2000). Aerodynamic Characteristics of Dragonfly Wing Sections Compared with Technical Aerofoils. Journal of Experimental Biology 203, 3125-3135.

Liu, H. (2009). Integrated modeling of insect flight: From morphology, kinematics to aerodynamics. Journal of Computational Physics 228, 439-459.

Maybury, W. J. and Lehmann, F.-O. (2004). The fluid dynamics of flight control by kinematic phase lag variation between two robotic insect wings. Journal of Experimental Biology 207, 4707-4726.

Miao, J. M. and Ho, M. H. (2006). Effect of flexure on aerodynamic propulsive efficiency of flapping flexible airfoil. Journal of Fluids and Structures 22, 401-419.

Nagai, H., Nishi, A., Fujimoto, T. and Isogai, K. (2009). Study on flow interaction mechanism of fore- and hindwings of dragonfly. In: Proceedings of the 4th International Symposium on Aero Aqua Bio-Mechanisms, Shanghai, China.

Nakata, T. (2009). Aerodynamic performance of flapping flexible wing in insect flight. Comparative Biochemistry and Physiology Part A: Molecular & Integrative Physiology 153, S50-S52.

Nakata, T. and Liu, H. (2009). Effects of structural flexibility on aerodynamic performance of flapping wing in insect flight. In: Proceedings of the 4th International Symposium on Aero Aqua Bio-Mechanisms Shanghai, China.

Okamoto, M., Yasuda, K., and Azuma, A. (1996). Aerodynamic Characteristics of the Wings and Body of A Dragonfly. Journal of Experimental Biology 199, 281-294.

Rival, D., Schonweitz, D. and Tropea, C. (2011). Vortex interaction of tandem pitching and plunging plates: a two-dimensional model of hovering dragonfly-like flight. Bioinspiration & Biomimetics 6.

Sane, S. P. and Dickinson, M. H. (2001). The control of flight force by a flapping wing: lift and drag production. Journal of Experimental Biology 204, 2607-2626.

Smith, M. J. C. and Zenieh, S. S. (1996). Trajectory Control of Flapping Wings: Towards the Development of Flapping-Wing Technology. In: AIAA, NASA, and ISSMO, 6th Symposium on Multidisciplinary Analysis and Optimization, Bellevue WA, USA. 493-500.

Somps, C. and Luttges, M. (1985). Dragonfly Flight: Novel Uses of Unsteady Separated Flows. Science 228, 1326-1329.

Srygley, R. B. and Thomas, A. L. R. (2002). Unconventional lift-generating mechanisms in free-flying butterflies. Nature 420, 660-664.

Sudo, S., Tsuyuki, K., Ikohagi, T., Ohta, F., Shida, S. and Tani, J. (1999). A Study on the Wing Structure and Flapping Behavior of Dragonfly. JSME International Journal Series C-Mechanical Systems, Machine Elements and Manufacturing 42, 721-729.

Sun, M. and Lan, S. L. (2004). A computational study of the aerodynamic forces and power requirements of dragonfly (*Aeschna juncea*) hovering. Journal of Experimental Biology 207, 1887-1901.

Sunada, S., Zeng, L. and Kawachi, K. (1998). The relationship between dragonfly wing structure and torsional deformation. Journal of Theoretical Biology 193, 39-45.

Thomas, A. L. R., Taylor, G. K., Srygley, R. B., Nudds, R. L. and Bomphrey, R. J. (2004). Dragonfly flight: free-flight and tethered flow viualisations reveal a diverse array of unsteady lift-generating mechanisms, controlled primarily via angle of attack. Journal of Experimental Biology 207, 4299-4323.

Tsuyuki, K., Sudo, S., and Tani, J. (2006). Morphology of Insect Wings and Airflow Produced by Flapping Insects. Journal of Intelligent Materials Systems and Structures 17, 743-751.

Wakeling, J. M. and Ellington, C. P. (1997). Dragonfly flight. II. Velocities, accelerations and kinematics of flapping flight. Journal of Experimental Biology 200, 557-582.

Walker, S. M., Thomas, A. L. R. and Taylor, G. K. (2009a). Deformable wing kinematics in free-flying hoverflies. Journal of The Royal Society Interface, Published online.

Walker, S. M., Thomas, A. L. R. and Taylor, G. K. (2009b). Deformable wing kinematics in the desert locust: how and why do camber, twist and topography vary through the stroke? Journal of The Royal Society Interface 6, 735-747.

Walker, S. M., Thomas, A. L. R. and Taylor, G. K. (2009c). Photogrammetric reconstruction of high-resolution surface topographies and deformable wing kinematics of tethered locusts and free-flying hoverflies. Journal of The Royal Society Interface 6, 351-366.

Wang, H., Zeng, L. and Liu, H. (2003). Measuring Wing Kinematics, Flight Trajectory and Body Attitude during Forward Flight and Turning Maneuvers in Dragonflies. Journal of Experimental Biology 206, 745-757.

Wang, J. K. and Sun, M. (2005). A computational study of the aerodynamics and forewing-hindwing interaction of a model dragonfly in forward flight. Journal of Experimental Biology 208, 3785-3804.

Wang, Z. J. (2000). Two Dimensional Mechanism for Insect Hovering. Physical Review Letters 85, 2216.

Wang, Z. J. (2005). Dissecting Insect Flight. Annual Review of Fluid Mechanics 37, 183-210.

Willmott, A. P. and Ellington, C. P. (1997). The mechanics of flight in the hawkmoth Manduca sexta. II. Aerodynamic consequences of kinematic and morphological variation. Journal of Experimental Biology 200, 2723-2745.

Wootton, R. J. (1992). Functional morphology of insect wings. Annual Review of Entomology 37, 113-140.

Wootton, R. J., Kukalová-Peck, J., Newman, D. J. S. and Muzón, J. (1998). Smart engineering in the mid-carboniferous: How well could palaeozoic dragonflies fly? Science 282, 749-751.

Xu, J., Zhao, C., Zhang, Y. and Zhang, Y. (2006). Effect of flapping trajectories on the dragonfly aerodynamics. Chinese Science Bulletin 51, 777-784.

Young, J., Walker, S. M., Bomphrey, R. J., Taylor, G. K. and Thomas, A. L. R. (2009). Details of Insect Wing Design and Deformation Enhance Aerodynamic Function and Flight Efficiency. Science 325, 1549-1552.